Combustion Theory and Modelling
Vol. 00, No. 00, Month 200x, 1–27

Large Eddy Simulation of a Bluff-body Stabilised Turbulent Premixed Flame using the Transported Flame Surface Density Approach

Chin Yik Lee[a]* Stewart Cant[a]

[a]*Department of Engineering, University of Cambridge, Cambridge, UK*

(*v4.2 released October 2009*)

A premixed propane-air flame stabilised on a triangular bluff-body in a model jet-engine afterburner configuration is investigated using large-eddy simulation (LES). The reaction rate source term for turbulent premixed combustion is closed using the transported Flame Surface Density (TFSD) model. In this approach, there is no need to assume local equilibrium between the generation and destruction of subgrid FSD, as commonly done in simple algebraic closure models. Instead, the key processes that create and destroy FSD are accounted for explicitly. This allows the model to capture large-scale unsteady flame propagation in the presence of combustion instabilities, or in situations where the flame encounters progressive wrinkling with time. In this study, comprehensive validation of the numerical method is carried out for non-reacting and reacting cases. The key physics of the flow field and the flame structure are also investigated in detail. For the non-reacting flow, good agreement for both the time-averaged and RMS velocity fields are obtained, and the Karman type vortex shedding behaviour seen in the experiment is well represented. For the reacting flow, two mesh configurations are used to investigate the sensitivity of the LES results to the numerical resolution. Profiles for the velocity and temperature fields exhibit good agreement with the experimental data for both the coarse and dense mesh. This demonstrates the capability of LES coupled with the TFSD approach in representing the highly unsteady premixed combustion observed in this configuration. Using the dense mesh, a larger fraction of turbulent kinetic energy is resolved and there is better resolution of local flame wrinkling, as manifested by a thinner flame front with higher localised FSD. The instantaneous flow pattern and turbulent flame behaviour are discussed, and the differences between the non-reacting and reacting flow are described through visualisation of vortical structures and their interaction with the flame. Lastly, the generation and destruction of FSD are evaluated by examining the individual terms in the FSD transport equation. Localised regions where straining, curvature and propagation are each dominant are observed, highlighting the importance of non-equilibrium effects of FSD generation and destruction in the model afterburner.

Keywords: Large eddy simulation; Turbulent premixed combustion; Transported flame surface density model, non-equilibrium effects of FSD generation and destruction

1. Introduction

Premixed turbulent combustion is a problem of considerable practical significance, for example in gas turbine combustors, spark-ignition engines, and accidental explosions. Much effort has therefore been devoted to gaining a better understanding of premixed flames to aid in the design of practical combustion systems. Recently, Large Eddy Simulation (LES) has emerged as the next-generation approach to improve this understanding via direct resolution of the large, energy-containing

*Corresponding author. Email: cyl36@cam.ac.uk

ISSN: 1364-7830 print/ISSN 1741-3559 online

DOI: 10.1080/13647830.YYYY.xxxxxx
http://www.tandfonline.com

scales of fluid motion [1]. LES holds advantages over traditional unsteady Reynolds-averaged Navier Stokes simulations (URANS) in situations where there is significant large-scale interaction between the turbulence and the flame structure, and has been used extensively in the prediction of thermoacoustic instabilities, reignition and extinction.

A central modelling challenge for LES of turbulent premixed combustion lies in the closure of the nonlinear chemical source term. Accurate subgrid-scale (SGS) models must be used to represent the chemical reactions occurring at molecular scales that cannot be resolved on LES meshes. Closures based on the flame surface density (FSD) concept [2, 3], flame wrinkling factor [4, 5], level-set equation [6, 7], presumed probability density function [8] or an artificially thickened flame approach [9] have been used. These approaches revolve around a key assumption that the chemical length-scales are much smaller than turbulence length-scales. This eventually leads to a problem of determining the unresolved surface area of the thin flame front and the burning rate per unit area of the corresponding flame surface.

The FSD concept describes the changes in the flame surface area as a result of flame front wrinkling due to turbulence, and has been studied extensively using Direct Numerical Simulation (DNS) [10]. The FSD can either be modelled using an algebraic closure or by solving a transport equation. An extension to the algebraic closure approach involves the use of dynamic models [11–14], where the model parameters are adjusted automatically in the simulation. In general, the algebraic FSD models rely on the assumption that subgrid flame area production and destruction rates are in equilibrium. By contrast, the derivation of the transported FSD models is based on theoretical considerations for a propagating surface as described by Pope [15] and Candel and Poinsot [16]. The equilibrium assumption is not required for the transported FSD model. Instead, the strain rate, propagation and curvature effects are explicitly accounted for. As such, the transported FSD approach is expected to have advantages over the simpler algebraic FSD approach in the description of cases involving high sugbrid flame wrinkling and unsteady flows with large-scale coherent structures [17].

In the present work, we adopt the transported FSD model proposed by Hawkes and Cant [2, 3] (TFSD). This model incorporates the filtered and subgrid terms for the production and destruction of the FSD. The key terms in FSD transport equation have been investigated via a-priori DNS studies to evaluate their effects on the flame structure at different Lewis number [18] and turbulent Reynolds number [19], and to quantify how these terms are appropriately represented within SGS modelling for LES [20]. This approach has also been extended and applied to flames in the corrugated flamelet and thin reaction zone regimes [17, 21]. Other modelling techniques involve solving the balance equation for the subgrid-scale flame wrinkling factor [5, 22], or solving the FSD balance equation but using a combustion filter that is larger than the LES filter width with appropriate models for the subgrid curvature and subgrid counter-gradient transport terms [23], are available. More recently, the transported approach has been used in LES studies of turbulent reacting flows including propagating flames [24], Bunsen flames [21, 25], swirled flames [23], bluff-body stabilized flames [5, 22, 24] and in IC engines [26]. The TFSD approach has been shown to provide superior predictions of the flame front evolution, flame height and curvature when compared against other state-of-the-art models without incurring excessive computational expense [25]. The TFSD model was also reported to outperform its algebraic counterparts in the thin reaction zone regime [21]. These studies have demonstrated that the TFSD approach can be implemented and applied to realistic, strongly wrinkled unsteady

flames with a good level of success.

The current work is motivated by the Volvo afterburner configuration consisting of a triangular bluff-body flameholder set within a rectangular duct [27–29]. The bluff-body generates a recirculation region that acts to facilitate flame stabilization. Further, the flame becomes highly unsteady towards the wake region as it is subjected to hydrodynamic instability and strong competition between baroclinc torque and fluid-mechanical straining [30, 31]. Complex dynamical behaviour involving distinct changes in the flame structure affected by the underlying flow field have also been observed when the operating conditions are varied [32]. A lean propane–air flame at equivalence ratio of $\phi = 0.6$ is considered. Information on the flame structure has been well-documented, and large amount of experimental data is available for this configuration using high speed imaging, gas analysis, Laser Doppler Velocimetry (LDV) and Coherent Anti-Stokes Raman Scattering (CARS) measurements [27–29]. There have also been several CFD studies for this configuration. Both steady [27] and unsteady [33] Reynolds Averaged Navier Stokes simulations have been carried out to analyse the temperature and CO profiles. LES has also been applied to assess and evaluate the accuracy of different subgrid-scale combustion modelling approaches [22, 24, 34–37]. Detailed assessment of the impact of numerics on the reacting flow results using different LES solvers [38] and evaluation of turbulence models in both URANS and LES [39] were also conducted. Many studies on this configuration focus on how large scale coherent structures modify the flame surface area and affect the chemical reaction rate [40], and also serve to investigate the changes of the flame dynamics in the presence of thermoacoustic oscillations [32, 41, 42].

In the present paper, the TFSD model is applied to the wake-stabilised premixed propane–air turbulent flame in the Volvo afterburner configuration.The aims of the study are to (i) provide a comprehensive and systematic validation of the thermochemical and fluid-mechanical properties in the Volvo rig, focusing on the mean and root mean square (RMS) fluctuating velocity profiles and the temperature fields; (ii) reproduce the physics of the flow field, with emphasis on the structural features and dynamical behaviour observed in both non-reacting and reacting flow and most importantly; (iii) investigate different terms in the FSD transport equation to identify the key mechanisms responsible for the generation and destruction of flame surface area on a local basis, and use these terms to highlight the physics of the flame structure when interacting with the underlying turbulent flow field.

2. Numerical Method

The governing equations for turbulent combustion LES are the Navier-Stokes equations for mass, momentum, and energy conservation. The Smagorinsky model [43] is used to solve for the subgrid stresses τ_{ij}

$$\tau_{ij} = -2\bar{\rho}(C_s\Delta)^2|\tilde{S}_{ij}|\tilde{S}_{ij} \tag{1}$$

where C_s is a model constant that takes a value of 0.1. The filter width Δ is taken as the cube root of the local mesh cell volume. The Favre-filtered rate of strain tensor $\tilde{S}_{ij}$ is

$$\tilde{S}_{ij} = \frac{1}{2}\left(\frac{\partial\tilde{u}_j}{\partial x_i} + \frac{\partial\tilde{u}_i}{\partial x_j}\right) \tag{2}$$

The term $|\tilde{S}_{ij}|$ represents the Frobenius form of the Favre filtered rate of strain tensor S_{ij} and takes the form

$$|\tilde{S}_{ij}| = \sqrt{2\tilde{S}_{ij}\tilde{S}_{ij}} \tag{3}$$

To account for the thermochemistry, the equation for the reaction progress variable c is solved

$$c = \frac{Y_F - Y_{FR}}{Y_{FP} - Y_{FR}} \tag{4}$$

where Y_F denotes the mass fraction of fuel, and the subscripts R and P indicate the reactants and the products, respectively.

The filtered progress variable is related to the density weighted progress variable using the expression [17]

$$\overline{c} = \frac{(1+\tau)\tilde{c}}{1+\tau\tilde{c}}\left[1 - \exp\left(-\Theta\frac{\Delta}{\delta_L}\right)\right] + \tilde{c}\exp\left(-\Theta\frac{\Delta}{\delta_L}\right) \tag{5}$$

where τ is the heat release parameter, Δ is the filter size, δ_L is the laminar flame thickness and Θ is a model constant that takes a value of 0.2 [17] for unity Lewis number flames.

The Favre-filtered transport equation for the progress variable is taken as

$$\frac{\partial\overline{\rho}\tilde{c}}{\partial t} + \frac{\partial(\overline{\rho}\tilde{u}_i\tilde{c})}{\partial x_i} + \frac{\partial}{\partial x_i}[\overline{\rho}(\widetilde{u_i c} - \tilde{u}_i\tilde{c})] = \overline{\frac{\partial}{\partial x_i}\left(\rho D\frac{\partial c}{\partial x_i}\right)} + \overline{\dot{\omega}} \tag{6}$$

The quantity D is the progress variable diffusivity. The terms in Eq. 6 in order from left to right are the unsteady term, convection term, subgrid flux of reaction progress variable, molecular diffusion term and chemical reaction rate. The subgrid scalar flux term is modelled using a gradient transport hypothesis [44]

$$\frac{\partial}{\partial x_i}[\overline{\rho}(\widetilde{u_i c} - \tilde{u}_i\tilde{c})] = \frac{\partial}{\partial x_i}\left(\frac{\mu_t}{\mathrm{Sc}_{sg}}\frac{\partial\tilde{c}}{\partial x_i}\right) \tag{7}$$

where μ_t is the turbulent viscosity and Sc_{sg} is the subgrid scale Schmidt number of 0.7. The combined reaction rate and molecular diffusion rate is given by [2]:

$$\overline{\frac{\partial}{\partial x_i}(\rho D\frac{\partial c}{\partial x_i})} + \overline{\dot{\omega}} = \overline{(\rho S_d)}_s\Sigma_{gen} = \rho_u S_L\Sigma_{gen} \tag{8}$$

where ρ_u the density of the unburnt mixture, S_L is the laminar flame speed and Σ_{gen} is the generalized FSD given by $\Sigma_{gen} = \overline{|\nabla c|}$ [10]. The transport equation for Σ_{gen} can be expressed as [2, 3]

$$\frac{\partial\Sigma_{gen}}{\partial t} + \frac{\partial(\tilde{u}_i\Sigma_{gen})}{\partial x_i} = -\frac{\partial}{\partial x_i}[\overline{(u_i)}_s - \tilde{u}_i]\Sigma_{gen}$$
$$+\overline{\left(S_d\frac{\partial N_i}{\partial x_i}\right)}_s\Sigma_{gen} - \frac{\partial}{\partial x_i}[\overline{(S_d N_i)}_s\Sigma_{gen}] + \overline{\left((\delta_{ij} - N_i N_j)\frac{\partial u_i}{\partial x_j}\right)}_s\Sigma_{gen} \tag{9}$$

where the terms on the RHS of Eq. 9 represent subgrid convection, curvature, propagation and tangential strain rate. The surface averaged flame normal $\overline{(N_i)}_s$ is expressed as

$$\overline{(N_i)}_s = -\frac{1}{\Sigma_{gen}}\frac{\partial \overline{c}}{\partial x_i} \tag{10}$$

The surface averaged displacement speed $\overline{(S_d)}_s$ is modelled as

$$\overline{(S_d)}_s = S'_L(1 + \tau c^*) \tag{11}$$

where τ is the heat release parameter, c^* is the progress variable at a given isosurface and S'_L is the modified flame speed incorporating the effects of straining and curvature that are dominant within the thin reaction zone regime [20], expressed as

$$S'_L = S_L - \frac{\rho D}{\rho_o}\frac{\partial \overline{(N_i)}_s}{\partial x_i} \tag{12}$$

The subgrid convection term accounts for scalar transport due to turbulent fluctuations and changes in velocity across a flame, and takes the form:

$$\begin{aligned}\frac{\partial}{\partial x_i}[\overline{(u_i)}_s - \tilde{u}_i]\Sigma_{gen} = &-\frac{\partial}{\partial x_i}\left(\frac{\nu_t}{\mathrm{Sc}_\Sigma}\frac{\partial \Sigma_{gen}}{\partial x_i}\right) \\ &-\frac{\partial}{\partial x_i}[(c^* - \tilde{c})\tau S_L \overline{(N_i)}_s \Sigma_{gen}]\end{aligned} \tag{13}$$

The turbulent Schmidt number for the FSD Sc_Σ is taken to be equal to Sc_{sg} (Eq. 7) [45]. The contribution of the propagation and curvature terms in Eq. 9 can be decomposed as [2, 3]:

$$\begin{aligned}-\frac{\partial}{\partial x_i}[\overline{(S_d N_i)}_s \Sigma_{gen}] + \overline{\left(S_d \frac{\partial N_i}{\partial x_i}\right)}_s \Sigma_{gen} \\ = P_{mean} + C_{mean} + C_{sg}\end{aligned} \tag{14}$$

where P_{mean} and C_{mean} are the resolved contributions of the propagation and curvature terms, while C_{sg} is the subgrid curvature term. The expressions for P_{mean} and C_{mean} are given as

$$P_{mean} + C_{mean} = -\frac{\partial}{\partial x_i}\left(\overline{(S_d)}_s \overline{(N_i)}_s \Sigma_{gen}\right) + \overline{(S_d)}_s \frac{\partial \overline{(N_i)}_s}{\partial x_i}\Sigma_{gen} \tag{15}$$

The expression for C_{mean} is chosen based on a-priori DNS [17]. The subgrid curvature acts as a destruction term proportional to Σ^2_{gen} [46] and is modelled as

$$C_{sg} = -\alpha\beta S_L \frac{\Sigma^2_{gen}}{1 - \overline{c}} \tag{16}$$

where $\alpha = 1 - \overline{(N_i)}_s \overline{(N_i)}_s$ is the resolution factor that tends to zero under fully resolved conditions and β is a model constant that takes a value of unity [17]. This

value was found adequate for the current configuration, and was selected through a preliminary study where β was increased from 1 to 3. When a larger β was used, the FSD magnitude was found to decrease. This is expected as the curvature term promotes destruction of the FSD for the modelling approach. A larger value above 2 was found to underpredict the FSD and affect the flame spread from LES compared to experiment.

The strain rate term describes the strain induced by the surrounding fluid on the flame and can be expressed as

$$\overline{\left((\delta_{ij} - N_i N_j)\frac{\partial u_i}{\partial x_j}\right)}_s = S_{mean} + S_{hr} + S_{sg} \tag{17}$$

where S_{mean} is the resolved contribution of the strain rate and S_{hr} is the strain rate due to heat release. The subgrid strain rate S_{sg} includes the subgrid contribution of strain rate effects due to both turbulence and heat release. The expressions for S_{mean} and S_{hr} are given as

$$S_{mean} + S_{hr} = [\delta_{ij} - \overline{(N_i N_j)}_s]\frac{\partial \tilde{u}_i}{\partial x_j} - (c^* - \tilde{c})\tau S_L \frac{\partial \overline{(N_i)}_s}{\partial x_i} \tag{18}$$

where $\overline{(N_i N_j)}_s$ is modelled as $\overline{(N_i N_j)}_s = \overline{(N_i)}_s \overline{(N_j)}_s + 1/3\delta_{ij}[1 - \overline{(N_k)}_s \overline{(N_k)}_s]$. The term S_{sg} is modelled as

$$S_{sg} = \Gamma\left(\frac{u'}{S_L}, \frac{\delta_L}{\Delta}\right)\frac{\sqrt{k}}{\Delta} \tag{19}$$

where Γ is an efficiency function which can be described using the Intermittent Net Flame Stretch (ITNFS) model [47]. The efficiency function proposed by Angelberger et al. [48] is used

$$\Gamma = 0.75 \exp\left[-\frac{1.2}{(u'_\Delta/S_L)^{0.3}}\right]\left(\frac{\Delta}{\delta_L}\right)^{2/3} \tag{20}$$

where u'_Δ is the turbulence intensity at the filter scale estimated using the Smagorinsky model according to the relation $u'_\Delta = \nu_t/C_s\Delta$, S_L is the laminar flame speed, Δ is the filter size and δ_L is the laminar flame thickness. The modelled transport equation for FSD [2, 3] takes the form below when the model for each term is incorporated

$$\begin{aligned}\frac{\partial \Sigma_{gen}}{\partial t} + \frac{\partial(\tilde{u}_i \Sigma_{gen})}{\partial x_i} &= \frac{\partial}{\partial x_i}\left(\frac{\nu_t}{Sc_\Sigma}\frac{\partial \Sigma_{gen}}{\partial x_i}\right) + [\delta_{ij} - \overline{(N_i N_j)}_s]\frac{\partial \tilde{u}_i}{\partial x_j}\Sigma_{gen} \\ &+\Gamma\frac{\sqrt{k}}{\Delta}\Sigma_{gen} - \frac{\partial}{\partial x_i}(\overline{(S_d)}_s \overline{(N_i)}_s \Sigma_{gen}) + \overline{(S_d)}_s \frac{\partial \overline{(N_i)}_s}{\partial x_i}\Sigma_{gen} - \alpha\beta S_L \frac{\Sigma_{gen}^2}{1-\overline{c}}\end{aligned} \tag{21}$$

The model is implemented in the open source CFD toolkit OpenFOAM [49]. The solver comprises a finite volume method, based on a compressible pressure based formulation using a collocated storage arrangement with Rhie and Chow [50] interpolation. In this work, the equations are discretized in space using a central differencing scheme which is second-order accurate in smooth regions of the solution and is flux limited in near steep gradients in order to guarantee boundedness. A

Crank–Nicolson time-stepping scheme is employed. The system of equations is solved using the PISO pressure correction algorithm [51]. The algorithm splits the solution procedure into an implicit predictor step followed by two corrector steps. In the predictor step, all quantities except the pressure are updated by solving the momentum, energy, reaction progress variable and FSD equation. In the corrector steps, the pressure Poisson equation is solved implicitly along with the equation of state to obtain the pressure, density and updated velocity fields that satisfy continuity. The density and updated velocity fields are then used to update other quantities including the energy, progress variable and FSD.

3. Configuration and Operating Conditions

The configuration corresponds to the Volvo afterburner experiment [29] (Fig. 1), which consists of a rectangular duct of size 1.0 m (length) $\times$ 0.12 m (height) $\times$ 0.24 m (width) containing an equilateral triangular bluff body of sides $w_f = 0.04$ m with one apex pointing into the reactant stream, located 0.318 m downstream from the inlet. The computational domain is divided into ten mesh blocks as shown in Fig. 1(b). Two different mesh counts of 5 and 10 million cells were tested and assessed. For the coarse mesh, the mesh count is 45 $\times$ 40 for blocks 1 and 2; 30 $\times$ 40 for blocks 3 and 4; 145 $\times$ 40 for blocks 5, 6 and 7; 160 $\times$ 40 for blocks 8, 9 and 10. For the dense mesh, the mesh count is 60 $\times$ 55 for blocks 1 and 2; 40 $\times$ 55 for blocks 3 and 4; 200 $\times$ 55 for blocks 5, 6 and 7; 210 $\times$ 55 for blocks 8, 9 and 10. The respective numbers of cells allocated along the spanwise direction of the domain for these two mesh densities are 120 and 140, respectively. As illustrated in Fig. 2, the mesh upstream of the bluff body is subjected to a gradual increment in expansion ratio in the axial direction. The mesh spacing around the bluff-body (blocks 3-7 in Fig. 1(b)) is refined to capture the local flame structure near the stabilization point. The aspect ratio for the mesh is kept small to avoid abrupt transitions that might affect the numerical solution.

The modified Borghi diagram is shown in Fig. 3 to provide an indication of the premixed combustion regime for the Volvo afterburner experiment. The flame has been reported to operate primarily within the corrugated flamelet regime, and extending slightly towards the lower limit of the thin reaction zone regime. The TFSD model in its current form is known to be capable of simulating the premixed flame for the combustion regimes considered in this study. The laminar flame speed is approximately 17.5 cm/s. For this mesh configuration, the mesh spacing of 0.8 mm (dense mesh) and 1.3 mm (coarse mesh) is prescribed in the flame stabilization region and locations where high shear is expected. Based on the estimated laminar flame thickness of 0.5-1.0 mm, the ratio of filter size to laminar flame thickness Δ/δ_L corresponding to the dense and coarse mesh is between 0.8-1.6 and 1.3-2.6, respectively. With the small grid sizes used in this work, the turbulent flame brush is resolved and no active control of flame thickness [26] is applied.

The inflow axial velocity of the fully premixed propane–air mixture was fixed at 17.3 m/s based on the inflow data reported in the experiment. The progress variable is set to zero at the inlet. The equivalence ratio is 0.6. A turbulence intensity of 4 % is specified at the inlet using an inflow turbulence generator [52]. The inlet temperature is 288 K, and a wave-transmissive boundary condition [53] is employed at the outlet. This boundary can be regarded as partially reflecting. The walls are treated as rigid, stationary, adiabatic and impermeable. As turbulent flames stabilised downstream of obstacles are known to be sensitive to thermal boundary conditions, predictions of the effective laminar flame speed and hence the reaction

may be affected in the wall region [54]. As such, specification of adiabatic boundary conditions for the walls is regarded as a simplification and must be interpreted with care. A zero gradient assumption is specified for the progress variable, temperature and pressure along the walls.

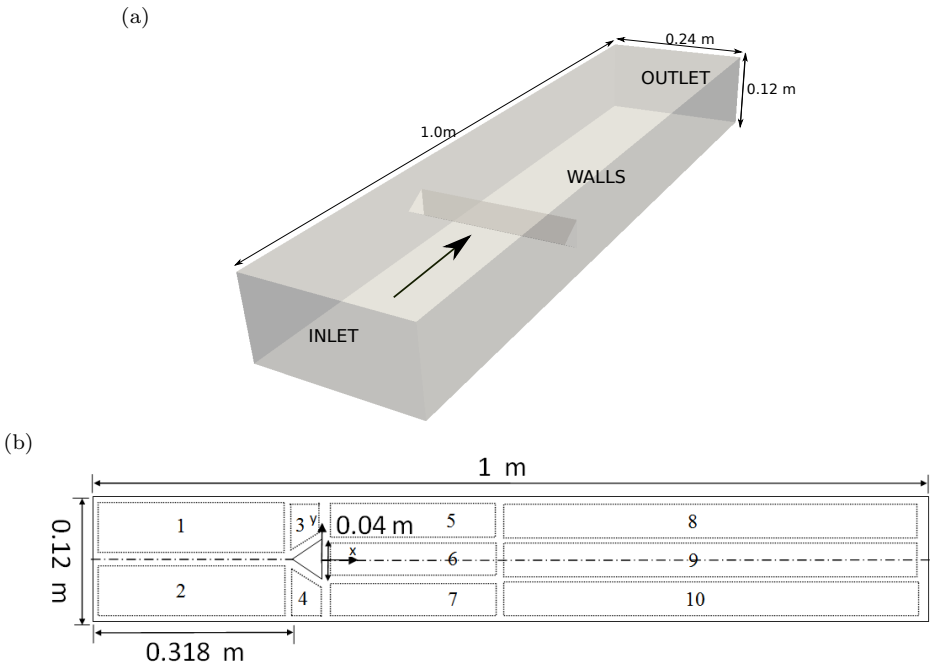

Figure 1.: Volvo afterburner geometry (a) and mesh arrangements (b)

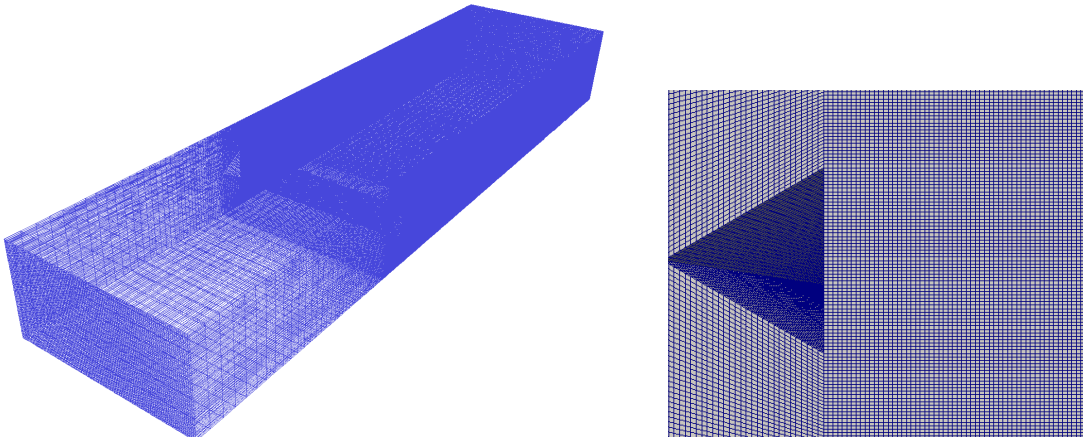

Figure 2.: 3D mesh for the Volvo afterburner geometry (left) and side view of the 3D mesh close to the flameholder (right)

For these studies, an adaptive timestep in the range of 5×10^{-8} - 1×10^{-7} s has been used. These values ensure a Courant–Friedrichs–Lewy (CFL) number less than 0.1 everywhere in the domain. The LES simulations are run for at least 30 characteristic time periods $\tau_b = w_f/u_{inlet}$ before the statistics are collected. The

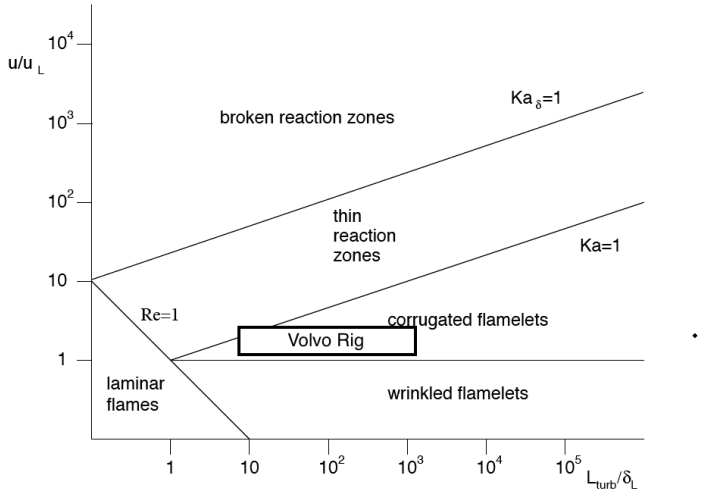

Figure 3.: Borghi diagram showing the combustion regime of the Volvo afterburner experiment

Favre-filtered variables from the simulation are gathered over 40 τ_b to obtain the statistics for the mean and second moment quantities.

4. Results

5. Cold Flow

Results from the non-reacting simulations are first presented to establish the validity of the mesh resolution, numerical discretization and subgrid-scale modelling for LES. In Fig. 4, the time-averaged axial velocity along the centreline downstream of the bluff body flameholder shows that both the strength and location of flow reversal are consistent with the experiment. The fluctuation level is presented in Fig. 5. Reasonable agreement with experimental data is also obtained for this quantity, suggesting that turbulent velocity fluctuations are adequately represented in the simulation.

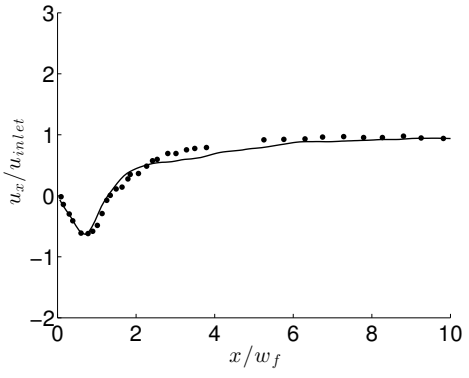

Figure 4.: Centreline time-averaged axial velocity profiles downstream of the bluff-body flameholder for non-reacting flow in LES

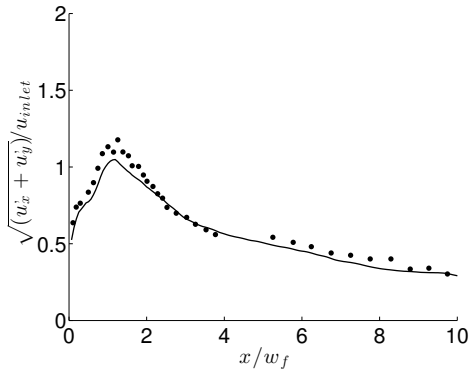

Figure 5.: Centreline fluctuation level profiles downstream of the bluff-body flameholder for non-reacting flow in LES

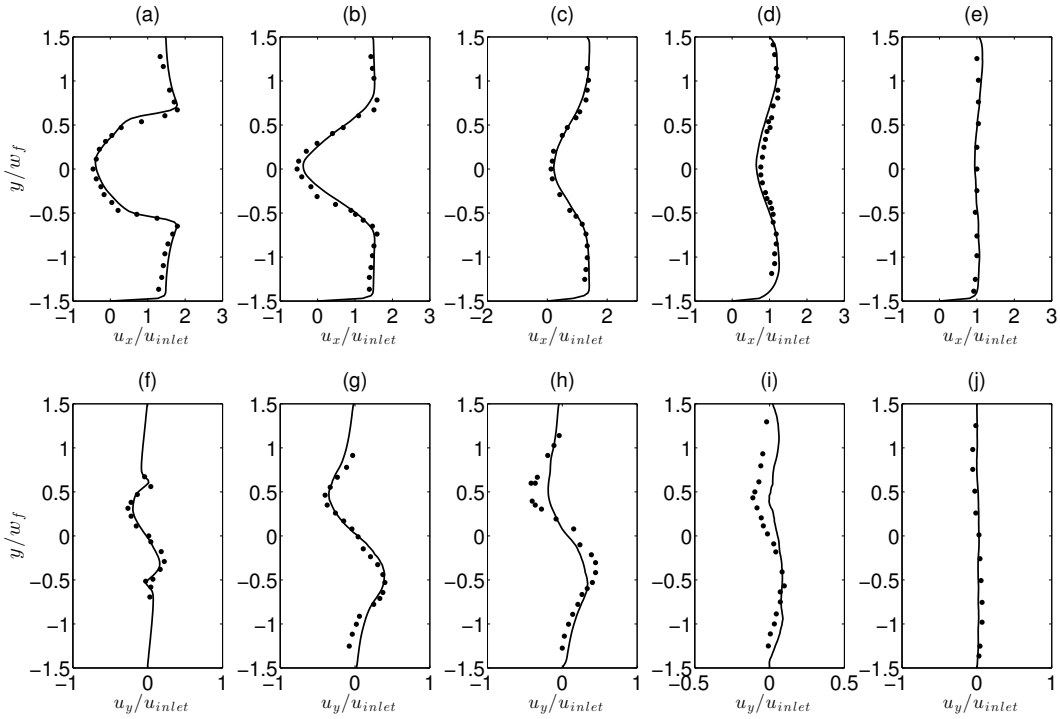

Figure 6.: Normalized axial (a-e) and transverse velocity (f-j) for the non-reacting flow at 0.375 w_f, 0.95 w_f, 1.5 w_f, 3.75 w_f and 9.4 w_f. Points: experimental data and solid lines: numerical results for LES

The time-averaged axial and transverse velocities at five different locations corresponding to 0.375 w_f, 0.95 w_f, 1.5 w_f, 3.75 w_f and 9.4 w_f are presented in the top and bottom rows in Fig. 6. The overall agreement between the experimental data and LES is good. The time-averaged axial velocity in Figs. 6(a-b) shows that a strong flow reversal is present immediately behind the bluff-body flameholder. Variations of mean transverse velocity are also present as distinct asymmetrical peaks can be seen on either side of the centreline in Fig. 6(f-i). The intensities of both the mean axial and transverse velocities remain high over a distance from

the flameholder of approximately 1.5 w_f. The strength of the velocity gradient reduces downstream at 9.4 w_f (Fig. 6e), where the axial velocity becomes more uniform. The mean transverse velocity also decreases after its peak value at 1.5 w_f as observed in Fig. 6(h). Slight discrepancies of the time-averaged velocities are found in the downstream region corresponding to 3.75 w_f, which may be due to the lower mesh resolution in the downstream region and the excess dissipation of the subgrid-scale model. The time-averaged fluctuating velocity components u'_{xx}, u'_{yy} and Reynolds stress are shown in the first, second and third rows in Fig. 7 respectively. The fluctuating velocities are normalized against the inlet velocity u_{inlet} and the Reynolds stress is normalized against u^2_{inlet}. The fluctuating quantities are also in agreement with the experimental data, suggesting that the subgrid-scale physics is well captured.

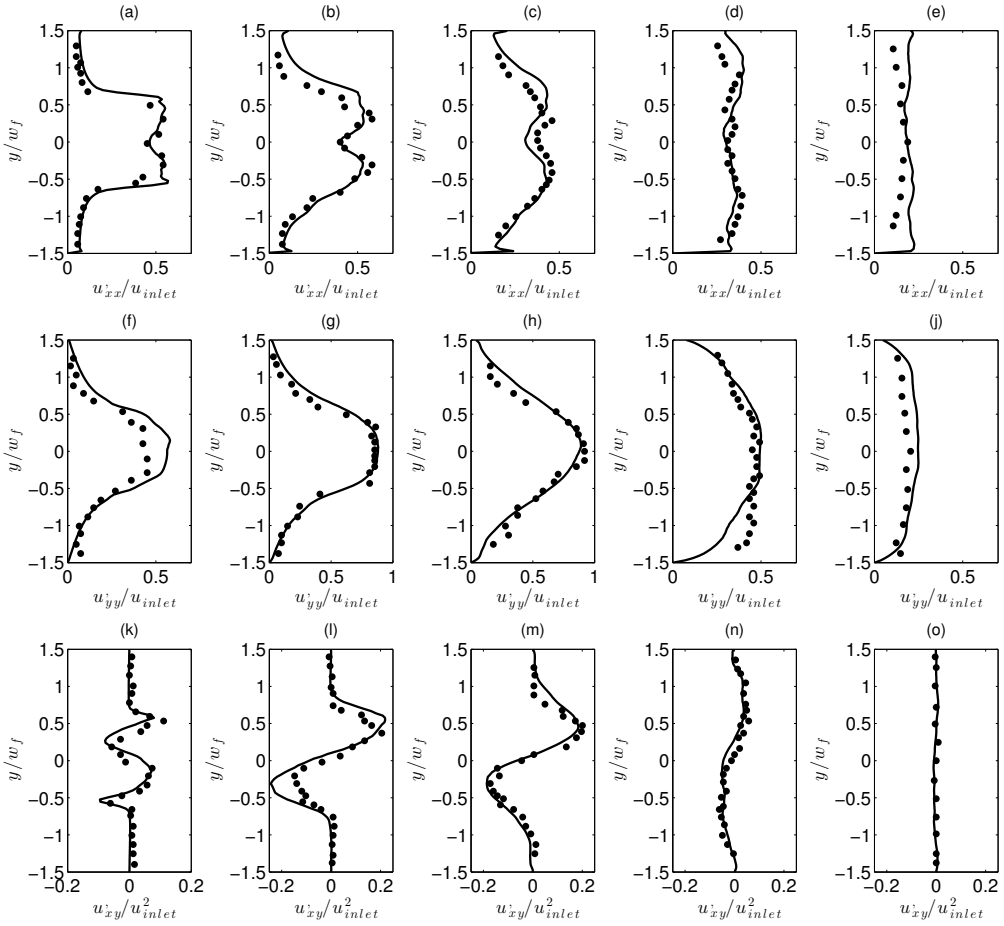

Figure 7.: Normalized fluctuating axial velocity (a-e), transverse velocity (f-j) and Reynolds stress (k-o) for the non-reacting flow at 0.375 w_f, 0.95 w_f, 1.5 w_f, 3.75 w_f and 9.4 w_f. Points: experimental data and solid lines: numerical results for LES

The instantaneous velocity field, pressure variation p' and vorticity magnitude for the non-reacting flow are shown in Fig. 8. The pressure variation is computed by subtracting the time-averaged value by its instantaneous value. Antisymmetrical Karman type vortex shedding is evident in Fig. 8a. Roll-up of the these vortical

structures occurs close to the flameholder in the recirculation region. From the p' contour (Fig. 8b), it is shown that large local pressure fluctuations are found close the bluff-body flameholder, in the vicinity of the recirculation zone and the flow reversal region. These pressure fluctuations are generated by the distorted flow structures of the vortices as they are being shed and due to their interaction. The vorticity magnitude contour in Fig. 8c shows that the vorticity is high close to the bluff body flameholder due to strong rotation of the flow as vortex shedding occurs. Further downstream the magnitude of vorticity decreases. Breakdown of vortices into smaller eddies and eventual dissipation due to stretching and viscosity effects can be seen at a distance downstream from the bluff-body flameholder.

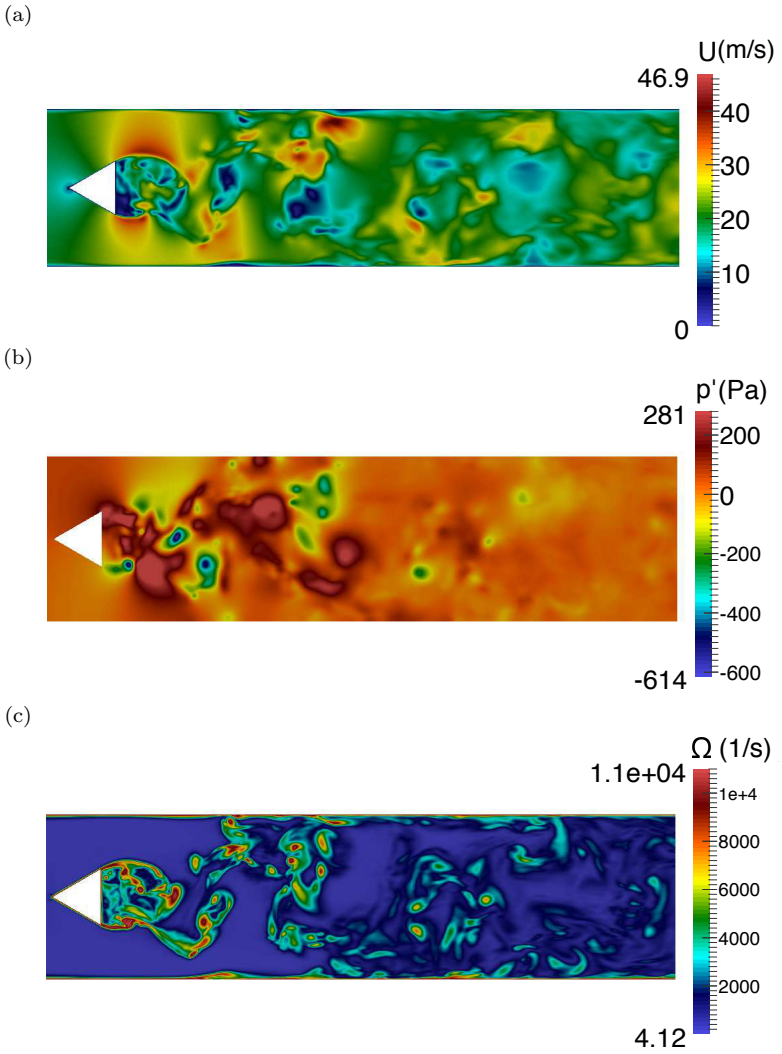

Figure 8.: (a) velocity magnitude [m/s] (b) pressure fluctuation [Pa] and (c) vorticity [1/s] of the non-reacting flow

The isocontour of the Q-criterion for the non-reacting flow at Q = 80000 s^{-1} is shown in Fig. 9. The Q-criterion is based on the definition by Hunt el al [55]. In Fig. 9, vortex shedding manifests itself as large-scale 'rollers' as the flow separates from the upper and lower edges of the bluff body. The structure of these 'rollers' is two-dimensional in nature as spanwise vortical variations are absent in the vicinity

of the bluff body flameholder. Breakdown of these large-scale vortical structures due to turbulence decay leads to smaller and less coherent vortices farther downstream.

The PSD of the turbulent kinetic energy for the non-reacting flow taken at the spatial location (x = 0.35 m, y = 0.06 m, z = 0.12 m) is shown in Fig. 10. The velocity fluctuations are first obtained by subtracting the mean values by the instantaneous velocities to compute the spectra. A base unit of unity is used as the reference value for dB conversion. The energy spectrum of the non-reacting flow shows a distinct peak at 102 Hz (Strouhal number = 0.25), which represents the alternate vortex shedding frequency and compares well with the experimental value of 105 Hz reported by Sjunnesson et al. [29]. The line plotted in the PSD plot indicates the slope of the turbulence spectrum of k = -5/3, where k represents the wavenumber. The recovery of this slope shows that the mesh is adequate for LES in the current study.

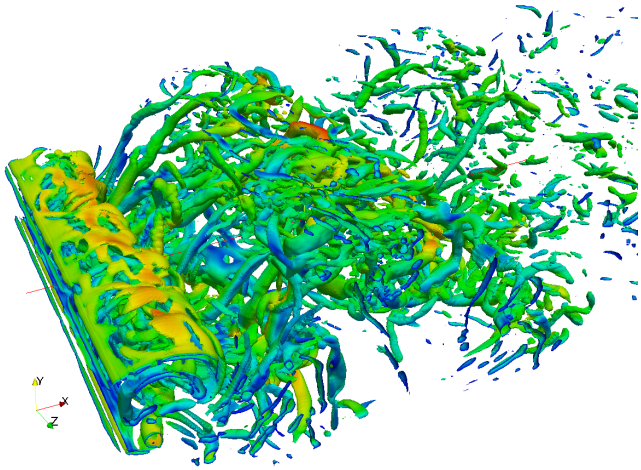

Figure 9.: Vortical structure of the non-reacting flow at Q = 80000 s^{-1}

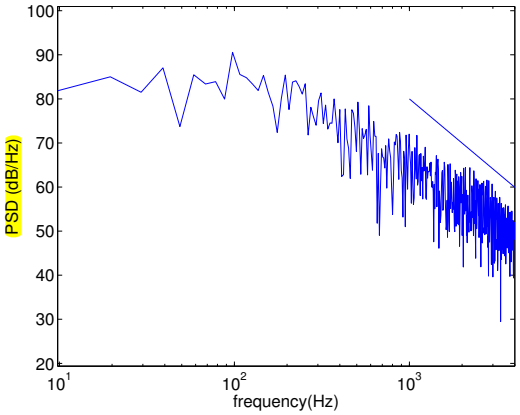

Figure 10.: PSD of the turbulent kinetic energy for the non-reacting flow

6. Reacting Flow

Comparison of the LES reacting flow results with the experimental data [27–29] is first performed for two different mesh counts of 5 million cells (coarse mesh) and 10 million cells (dense mesh) to examine the validity of the mesh topology employed. Results for the dense mesh and coarse mesh are indicated by the solid and dotted lines, respectively. As shown in Fig. 11, the profile of the time-averaged centreline axial velocity compares well with the experiment. In particular, the location of the minimum is well captured, demonstrating that the recirculation zone length is predicted adequately. The increase in the recirculation zone length in the reacting flow compared to the cold flow is associated with volumetric expansion caused by chemical heat release. From Fig. 12, it can be seen that that a reasonable estimation of the turbulent fluctuation level downstream of the bluff body is also obtained, and a slight overprediction can be observed in the vicinity of the flow reversal region for both coarse and dense mesh configurations. As demonstrated previously [38], accurate prediction of the turbulent fluctuation level is especially challenging for reacting flows. As the most of the flow is resolved, the overprediction observed here is most likely due to the subgrid-scale modelling. In this region, strong turbulence-flame interactions are expected to occur. Given that the flow is highly unsteady close to the shear layer and flow reversal region, it is likely that the turbulence fluctuations are high in these locations and can be overestimated by the subgrid-scale turbulence model.

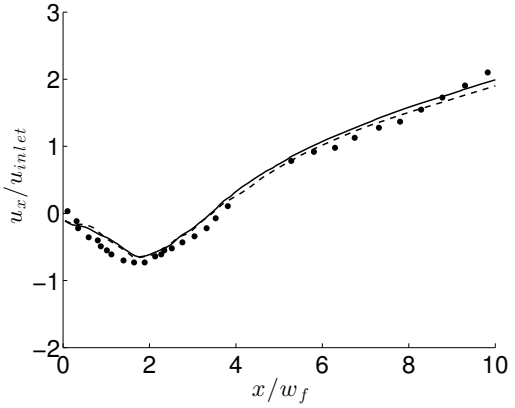

Figure 11.: Centreline time-averaged axial velocity profiles downstream of the bluff-body flameholder for reacting flow in LES. Points: experimental data, solid lines: dense mesh, dotted lines: coarse mesh

The time-averaged axial and transverse velocity profiles at 5 different axial locations corresponding to 0.375 w_f, 0.95 w_f, 1.5 w_f, 3.75 w_f and 9.4 w_f are presented in Fig. 13. The axial velocity (top row) and transverse velocity (bottom row) are normalized against the inlet velocity u_{inlet}. The time-averaged fluctuating velocity components u'_{xx}, u'_{yy} and Reynolds stress are obtained at the same locations as the mean values are shown Fig. 14. The fluctuating velocities are normalized against u_{inlet} and the Reynolds stress is normalized against u^2_{inlet}. As can be seen in Fig. 13, the trend for the time-averaged axial and transverse velocity for both coarse and dense meshes is well represented using LES, and the agreement with experimental data is good. The normalized time-averaged axial velocity indicates that the recirculation zone remains prominent up to a downstream distance of 3.75

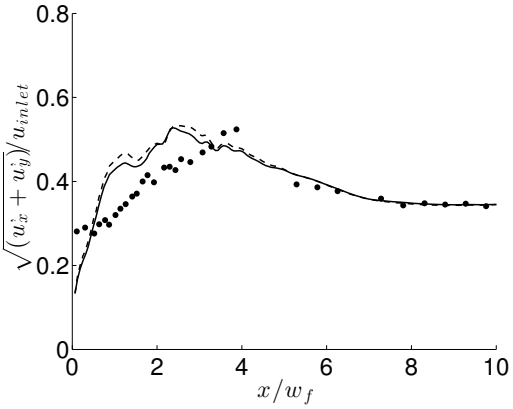

Figure 12.: Centreline fluctuation level profiles downstream of the bluff-body flameholder for reacting flow in LES. Points: experimental data, solid lines: dense mesh, dotted lines: coarse mesh

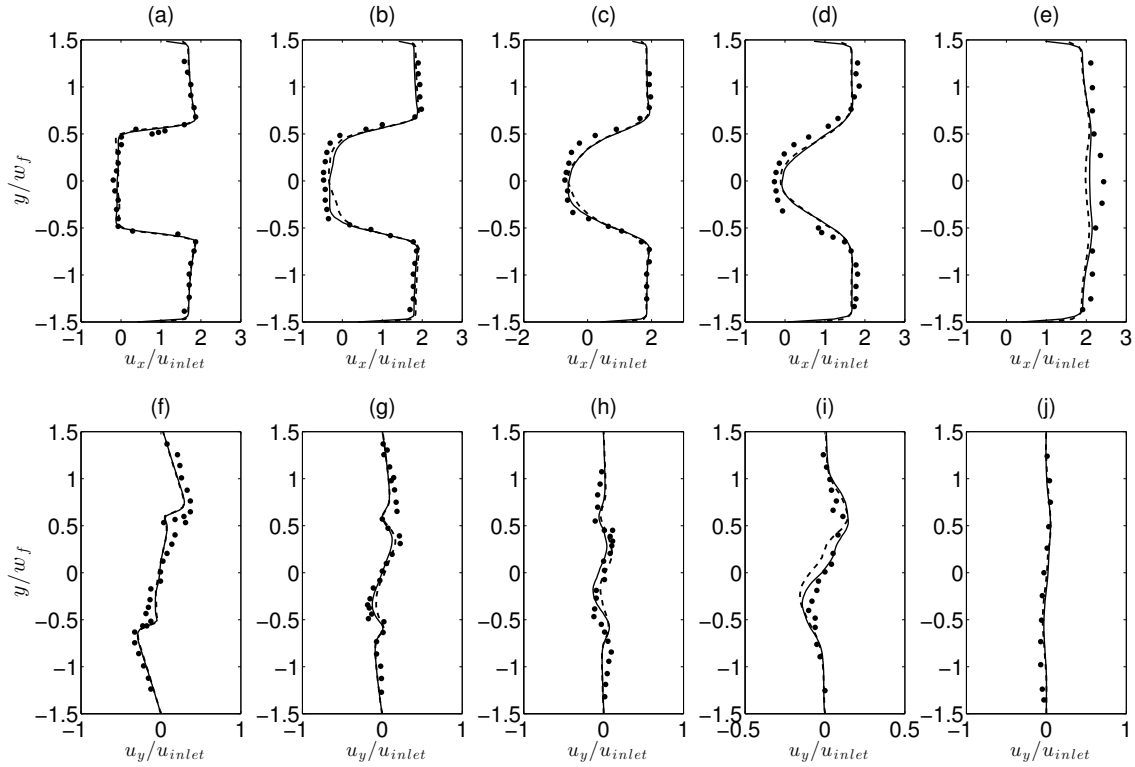

Figure 13.: Normalized axial (a-e) and transverse velocity (f-j) for the reacting flow at 0.375 w_f, 0.95 w_f, 1.5 w_f, 3.75 w_f and 9.4 w_f. Points: experimental data, solid lines: dense mesh, dotted lines: coarse mesh

w_f (Fig. 13d). The axial velocity in the downstream region is approximately 2.5 times larger than the inlet flow velocity as a consequence of the heat release in the wake, as shown in Fig. 13(e). The region of flow reversal, indicated by the width of the low axial velocity region, is also wider than in the non-reacting case. In

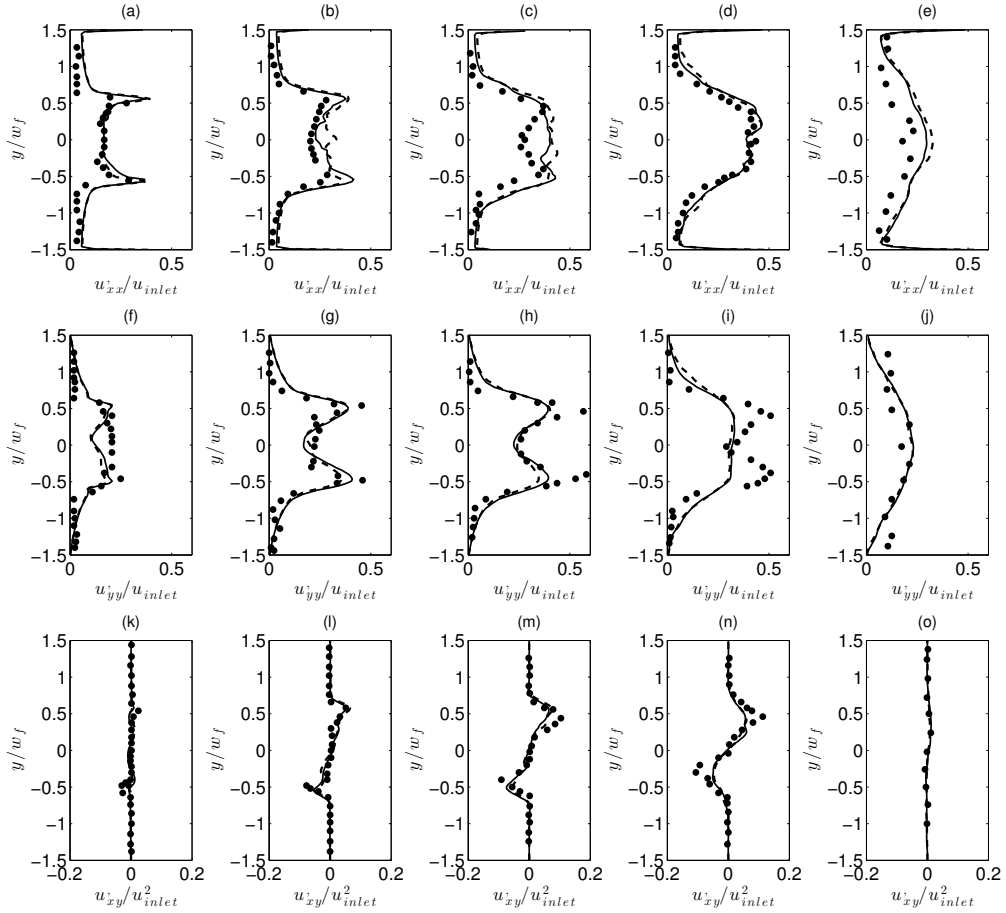

Figure 14.: Normalized fluctuating axial velocity (a-e), transverse velocity (f-j) and Reynolds stress (k-o) for the reacting flow at 0.375 w_f, 0.95 w_f, 1.5 w_f, 3.75 w_f and 9.4 w_f. Points: experimental data, solid lines: dense mesh, dotted lines: coarse mesh

Figs. 13(f-i), the magnitudes of the normalized time-averaged transverse velocity are much lower than in the non-reacting flow. This is caused by thermal expansion and baroclinicity which create a stabilizing effect on the hydrodynamics of the flame [30, 56]. Another notable aspect of the normalized transverse velocity is the inflection point in the shear layers around the flame stabilization region. This can be seen in the region of y = 0.5 and y = -0.5 in Fig. 13(f) and (g). This behaviour corresponds to the rapid change in velocity across the flame front, which does not exist under non-reacting conditions. This effect dissipates further downstream. The fluctuating quantities for both cases also compare well with the experimental data. Slight discrepancies in the fluctuating velocity components with experiment are however evident in the flow reversal and wake region (Fig. 14c,h,i) where the flow is highly unsteady.

Results for the mean temperature profiles at three downstream locations 3.75 w_f, 8.75 w_f and 13.75 w_f are depicted in Fig. 15. The temperature is normalized by the inlet value and the distance by the bluff body width w_f. Close to the flameholder,

the time-averaged temperature profiles taken at all three different locations match well with experimental data. Further downstream, the maximum value of the time-averaged temperature is consistent with the experiment but the spreading rate of the time-averaged temperature profile is slightly underestimated.

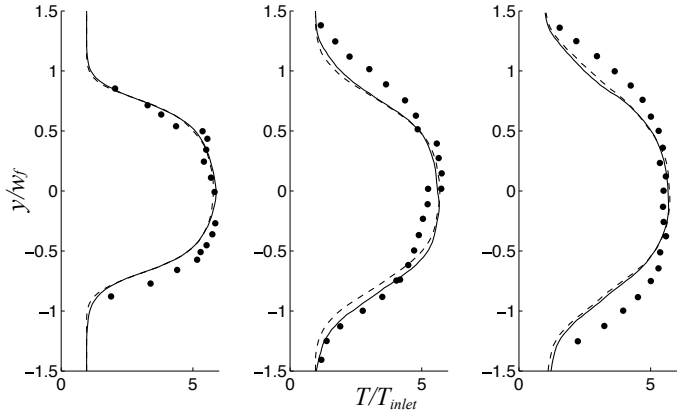

Figure 15.: Normalized temperature profile at 3.75 w_f, 8.75 w_f and 13.75 w_f. Points: experimental data, solid lines: dense mesh, dotted lines: coarse mesh

The quality of any LES simulation is dependent on the percentage of the resolved turbulent kinetic energy. For high Reynolds number flows, Celik et al. [57] considered that resolving 70 to 85 % of turbulent kinetic energy is sufficient. To evaluate the quality of the reacting flow LES results between the two different meshes, the resolved fraction of the TKE $k_r = k_{res}/(k_{res}+k_{sgs})$ is used [58]. The resolved TKE k_{res} is evaluated using $1/2\sum(u_i-\tilde{u}_i)^2$ and the subgrid scale TKE k_{sgs} is estimated using the Smagorinsky model as $\nu_{sgs}/(C_s\Delta)^2$. In this formulation, the value of k_r is bounded between zero and unity, where larger values of k_r correspond to the resolution of more of the turbulent motions. Figure 16 shows that for a large portion inside of the domain, more than 85% of the turbulent kinetic energy are resolved for both the dense and coarse mesh. Only in the regions close to the separated shear layer and along the wall, the resolution decreases. It was also found that the dense mesh captures a higher percentage of the total turbulent kinetic energy compared to the coarse mesh that contains more localized regions of low k_r.

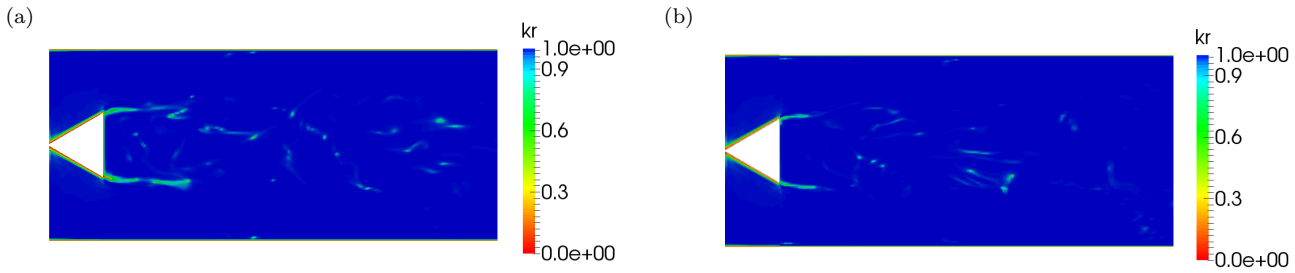

Figure 16.: Values of k_r for 5 million cells (a) and 10 million cells (b)

The time-averaged FSD contours for both the dense and coarse mesh are presented in Fig. 17. It can be seen that the time-averaged FSD profiles are quantitatively and qualitatively similar for both mesh resolutions. A slightly thicker

flame brush and lower values of FSD towards the downstream region are predicted when a lower mesh count of 5 million cells is used. This can be seen more clearly through the profiles of the time-averaged FSD normalised by its maximum value for both cases at 0.375 w_f, 0.95 w_f, 1.5 w_f, 3.75 w_f and 9.4 w_f shown in the bottom row of Fig. 17. Such results are expected since the reduction in mesh resolution would smear out the flame area, reducing the extent of wrinkling and increasing the turbulent flame thickness. Nevertheless, the consistency in the results for both the dense and coarse mesh, and the good agreement with the experimental data presented earlier demonstrates both the adequacy of the TFSD model in capturing the flow field and flame structure.

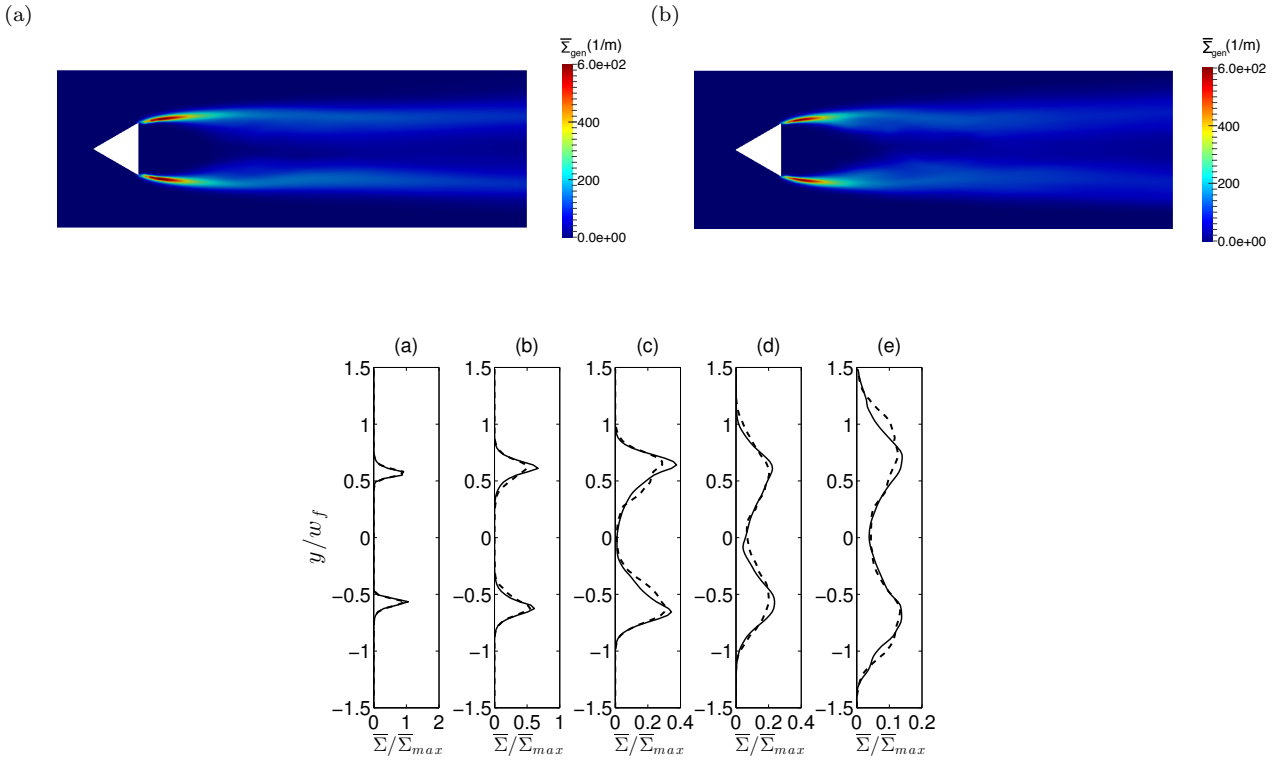

Figure 17.: Time averaged FSD [1/m]: dense mesh (top a), coarse mesh (top b), time-averaged FSD for both cases at 0.375 w_f, 0.95 w_f, 1.5 w_f, 3.75 w_f and 9.4 w_f (bottom). Solid lines: dense mesh, dotted lines: coarse mesh

Contours of instantaneous velocity magnitude, temperature, vorticity magnitude and reaction rate of the flame are shown in Fig. 18. The reaction rate is taken as $\rho_u S_L \Sigma_{gen}$ for the TFSD model. The flow field of the reacting flow is distinctively different from the non-reacting condition. As shown in Fig. 18a, a low velocity region is present in the recirculation zone. Symmetrical vortex shedding occurs immediately downstream of the flow reversal region. A strong velocity gradient can also be seen across the mixing layer around the recirculation zone as a result of density variation. The flow acceleration further downstream closer to outlet of the enclosure is a consequence of the sudden flow expansion from combustion heat release. The flame in Fig. 18b is represented by a steep gradient of temperature, and can be visualized as sheet-like structures emanating from the upper and lower edges of the flameholder. The flame lies almost parallel to the separating flow introducing a baroclinic torque which will tend the counter the effect of the fluid-mechanical

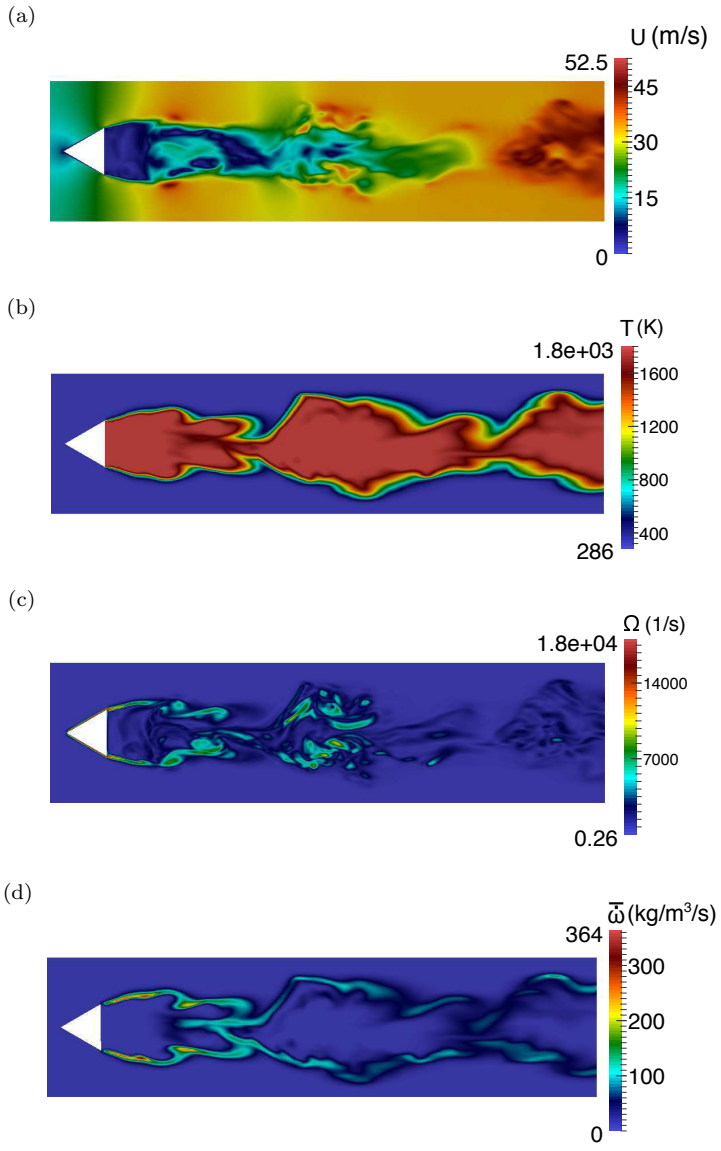

Figure 18.: Contours of velocity magnitude [m/s] (a), temperature [K] (b), vorticity magnitude [1/s] (c) and reaction rate [kg/m^3/s] (d) for the turbulent premixed flame

rotation due to vortex shedding. This suppresses the Karman-type instability that is present in the non-reacting flow, resulting in a symmetrical flame structure. Also, an increase in the flame surface area can be seen as the flame is stretched and entrained by vortices downstream of the vortex core. In Fig. 18c, the vorticity is high along the separating shear layer but is much lower in the vortex core where the flame stabilizes. Distorted vortical structures are also present where the flow reversal occurs, as indicated by high magnitude of vorticity. High reaction rates are found along the separated shear layers immediately downstream of the flameholder (Fig. 18d). The intensity of the reaction rate decreases further downstream towards the wake.

The PSD of the turbulent kinetic energy for the reacting flow, taken at the spatial location (x = 0.35 m, y = 0.06 m, z = 0.12 m), is shown in Fig. 19. The

PSD is obtained using the same methodology as the non-reacting flow. The energy spectrum in the reacting flow reveals a dominant frequency of 137 Hz (Strouhal number = 0.316) and its first harmonic at 370 Hz, which correlates well the the symmetrical shedding frequency reported in previous work [22, 34, 35].

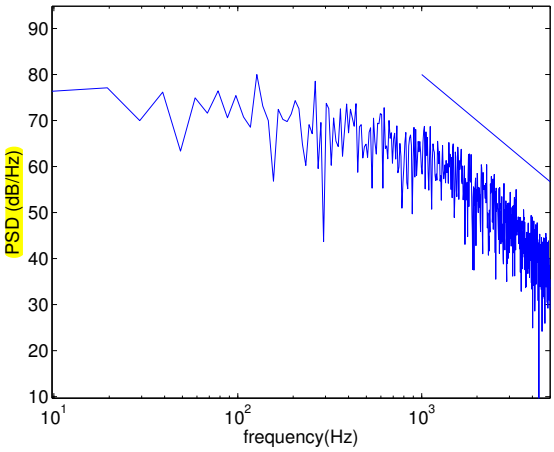

Figure 19.: PSD of the turbulent kinetic energy for the reacting flow

The Q-criterion at isosurface Q = 200000 s^{-1} is depicted in Fig. 20a. A symmetrical vortex sheet is formed in the upper and lower mixing layer behind the bluff body. Downstream of the vortex sheet, a pair of stationary vortices forms at the top and bottom edges (region 1). Immediately downstream of the counter-rotating vortex pair (region 2), the onset of a 'zig-zag'-like secondary instability [56] is present. This instability indicates the breakdown of the symmetrical mode and is characterized by the wavy vortex structure in the spanwise direction. This undulating structure is out-of-phase between the upper and lower shear layers and possesses a distinctive lengthscale in the spanwise direction. Such a structure is not present in the non-reacting flow. Further downstream (region 3), vortex stretching leads to elongated vortical structures whilst small-scale vortices are formed due to breakdown of larger vortices. Horseshoe vortices can also be seen in the wake region.

The isocontour of the Favre-filtered progress variable = 0.5 coloured according to the vorticity magnitude is shown in Fig. 20b to illustrate the interaction of vortical structures with the flame. The flame is inherently two-dimensional close to where the vortex sheets are continuously shed off the upper and lower lips of the flameholder (region 1). Further downstream (region 2), flow reversal occurs and the vorticity magnitude is high. The location where strong flow reversal occurs is consistent with where the wavy vortex structures are formed. Downstream of the flow reversal (region 3), breakdown of the spanwise vortices can be seen. The flame becomes strongly wrinkled and a staggered pattern develops due to vortex-vortex and flame-vortex interactions. The transition into the staggered pattern depends on where the secondary instability occurs, and affects the length of the recirculation zone [40]. As the flame develops downstream it propagates normal to itself, causing negatively curved wrinkles to contract and positively curved wrinkles to expand when affected by the local flow variations. This kinematic restoration process is strongly nonlinear and tends to control the decay of the flame response to flow oscillation [59, 60].

Physical insight into the flame can be obtained by analyzing the individual terms

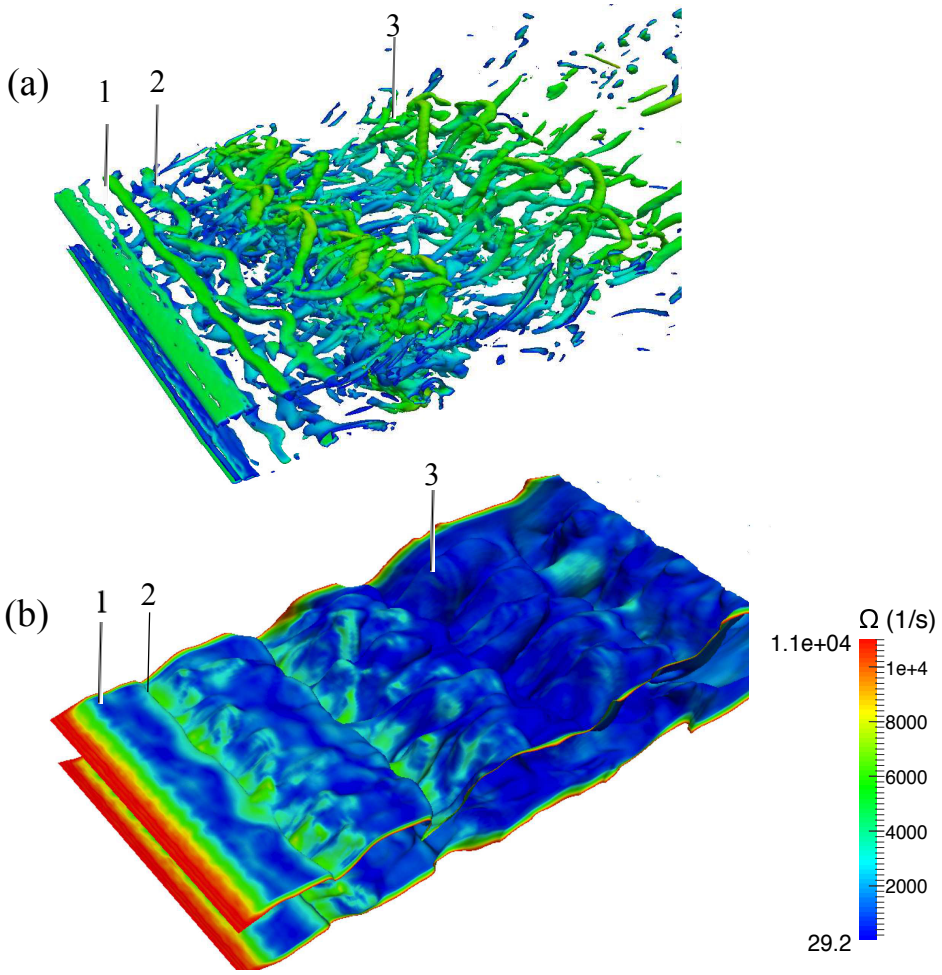

Figure 20.: (a) Vortical structure of the reacting flow at Q = 200000 s^{-1} and (b) isosurface of the progress variable at 0.5 coloured according to the vorticity magnitude

in the transport equation for Σ_{gen} in the TFSD model (Eq. 21). These terms dictate the local generation and destruction of the FSD and hence govern the structure and dynamic behaviour of the flame. Fig. 21 depicts the (a) resolved propagation and curvature, (b) resolved straining, (c) subgrid curvature and (d) subgrid straining for the TFSD model. Different regions downstream of the flameholder are denoted by R1 (flameholder lip) R2 (shear layer), R3 (flow reversal) and R4 (wake), respectively. Close to the flameholder (R1 and R2), the resolved propagation term (Fig. 21a) is seen to be low on the products side of the shear layer and high towards the reactants. This term takes positive values in the fresh gases and negative values in the burnt gases. The resolved strain term (Fig. 21b) is high in the localised region where the flow separates from the flameholder lip (R1) and can be seen to take positive and negative values along the shear layer (R2 and R3). The latter indicates that the flame front undergoes both compressive and extensive straining due to vortex rollup along the shear layer where the flame resides. The subgrid curvature term (Fig. 21c) is high in the shear layer (R2) and in the vicinity of flow reversal (R3) in both the upper and lower branches of the flame. Interactions and small-scale annihilations of flame elements occur in these regions. High subgrid strain (Fig. 21d) can be seen in the flow separation region especially at the edges

of the bluff body (R1) and along the flame front downstream of the recirculation zone (R2) where the flame is highly stretched by vortices. Its magnitude decreases further downstream.

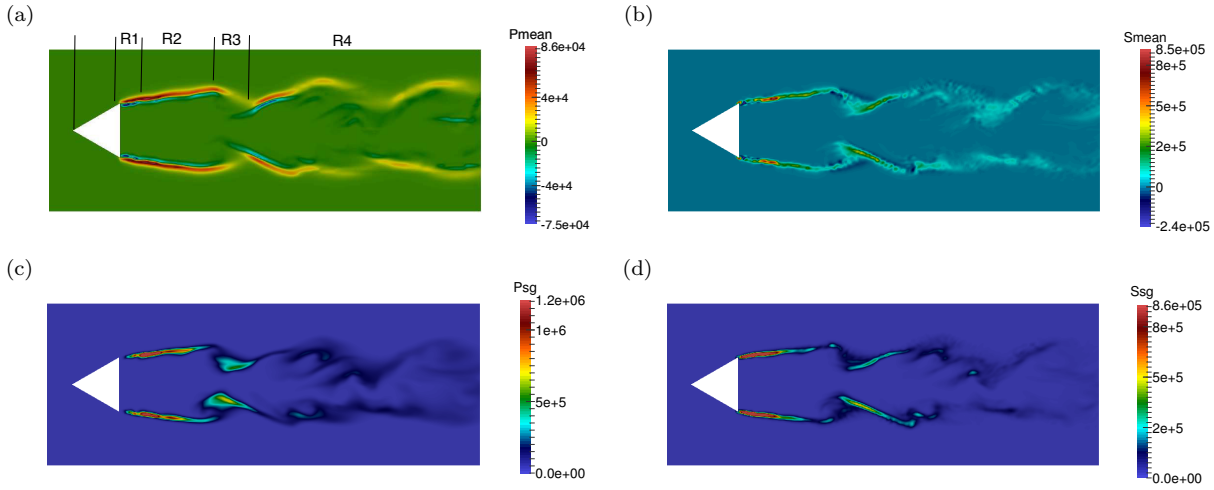

Figure 21.: (a) resolved propagation and curvature, (b) resolved straining, (c) subgrid curvature and (d) subgrid straining for the TFSD model

The instantaneous contours for each term in the FSD transport equation taken at $\tilde{c} = 0.5$ are presented in Fig. 22 to complement the side views and illustrate the spanwise variations. High magnitudes of both the resolved propagation term (Fig. 22a) and resolved strain rate term (Fig. 22b) can be seen primarily in the separated shear layer and flow reversal region. Localised regions of high values of the resolved propagation term (Fig. 22a) are also observed in the wake where bulging of the flame is present. The subgrid curvature term is dominant in the shear layer close to the recirculation zone and in the vicinity of the flow reversal. The subgrid straining is found to be high in the flow separation region of the bluff body lip. These observations are consistent with those shown in the side view in Fig. 21. The contours also show that spanwise variations of each term are fairly small near the flameholder, but tend to become more significant downstream in the wake.

The time-averaged side view contours of individual terms in the FSD transport equation are presented in Fig. 23. These contours show that generation and destruction of flame surface area occur primarily in the flow separation region around the flameholder lip and in the shear layer. These effects become less evident further downstream. Both the time-averaged resolved propagation and curvature term (Fig. 23a) and the resolved contribution of tangential strain rate term (Fig. 23b) are dominant close to the bluff-body where the flame stabilises. The extent of flame surface evolution in the subgrid-scales is also found to be more prevalent compared to the resolved-scales especially in the separated shear layers, as indicated by higher magnitudes of time-averaged subgrid curvature (Fig. 23c) and subgrid strain rate (Fig. 23d). This is expected as small-scale vortical structures affecting the subgrid flame surface area are present in the vicinity of the bluff-body flameholder. It can also be seen that the magnitude of time-averaged subgrid curvature (Fig. 23c) is largest slightly downstream of the bluff-body compared to the time-averaged subgrid strain rate that is dominant at the edges of the bluff-body.

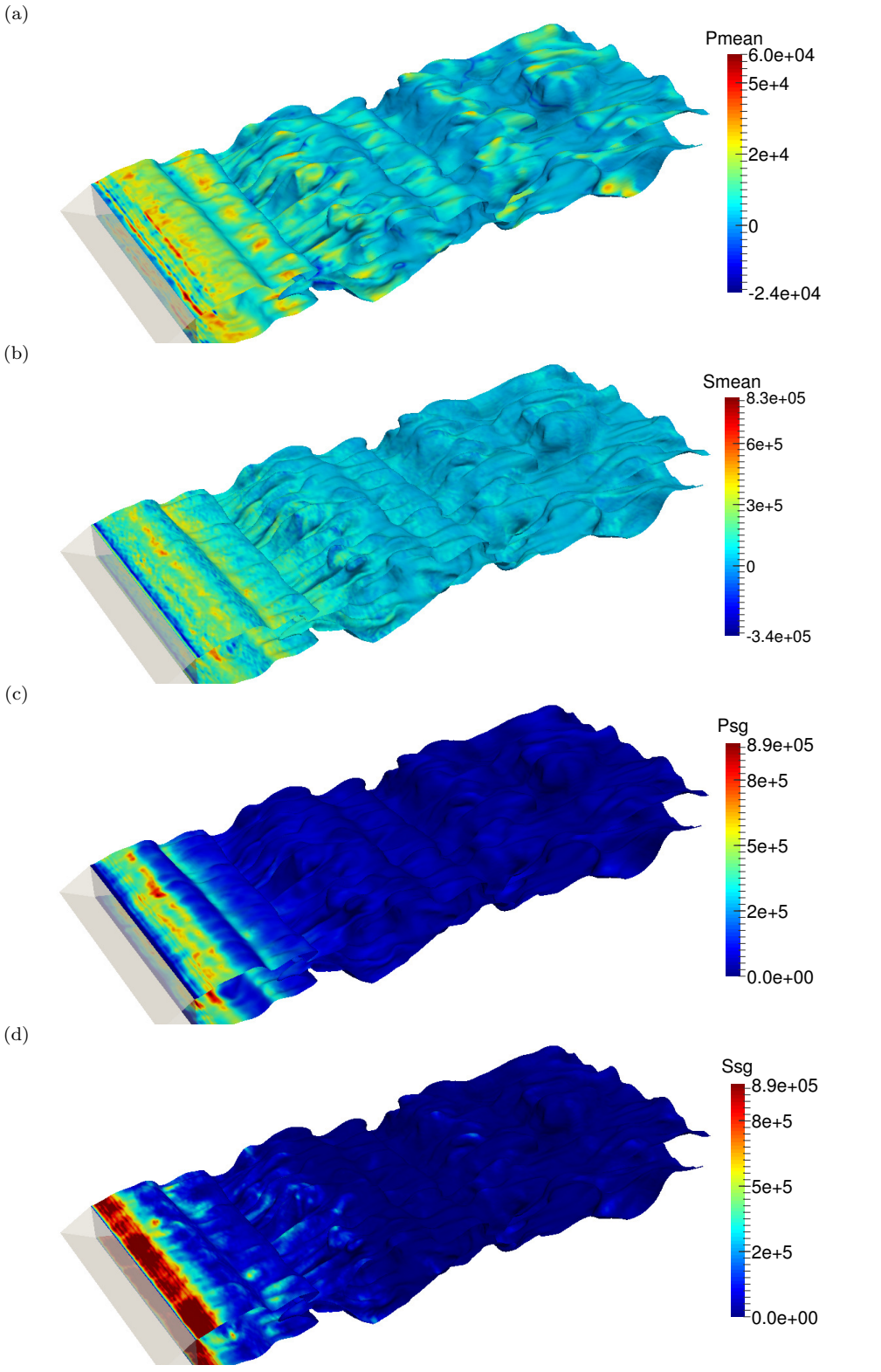

Figure 22.: Contours of the (a) resolved propagation and curvature, (b) resolved straining, (c) subgrid curvature and (d) subgrid straining for the TFSD model at $\tilde{c} = 0.5$

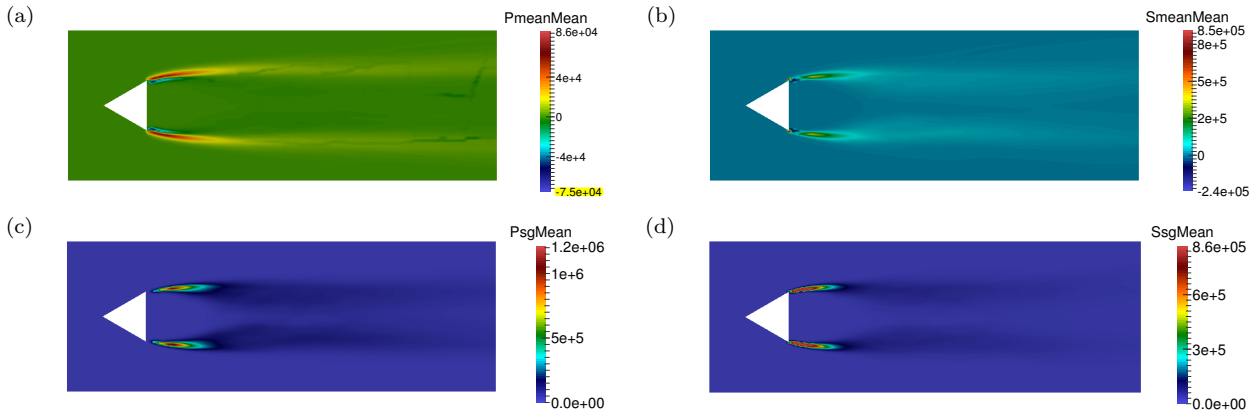

Figure 23.: Time-averaged values of (a) resolved propagation and curvature, (b) resolved straining, (c) subgrid curvature and (d) subgrid straining for the TFSD model

The use of the TFSD approach to combustion modelling enables the physics of the flame to be revealed through individual terms in the FSD transport equation. The results demonstrate that straining acts mainly as a source for FSD generation while propagation and curvature mainly act as sink for the FSD. It is found that generation of FSD occurs primarily in the flow separation region at the bluff-body edges and along the shear layer. The FSD destruction, on the other hand, concentrates both in the shear layer farther away from the flameholder and in the flow reversal zone. Destruction of the FSD is found to occur predominantly at the subgrid scales instead of the large-scales. The resolved local propagation effects were also found to be important especially in the shear layer of the recirculation zone. It is found that, in general, the strength of these terms decreases towards the downstream wake region.

7. Conclusions

A turbulent lean premixed propane–air flame with a triangular bluff-body stabiliser was simulated using the TFSD model in the context of Large Eddy Simulation. A validation of the non-reacting flow has demonstrated the adequacy of the mesh resolution and subgrid-scale turbulence model used. The flow features pertaining to the large-scale vortex shedding and its hydrodynamic frequency at 105 Hz were also well predicted. For the reacting flow, the TFSD LES results showed overall good agreement with the experimental data. The mean and fluctuating velocities along the centreline and at different spatial locations of the combustion chamber matched well with the experiment. The time-averaged temperature profile also attained reasonable agreement with the experimental data. An assessment of the LES quality based on the measure of resolved turbulent kinetic energy, as well as as consistency in the time-averaged FSD profiles between the coarse and dense meshes, demonstrated that appropriate resolution was achieved. LES revealed a symmetrical flame structure under reacting conditions, in contrast to the asymmetric vortex shedding observed in the non-reacting flow. When combustion is present, a convectively unstable shear layer characterized by alternating vortex pairs can be seen close to the flameholder, followed by spanwise vortex evolution in the downstream region.

By using the TFSD model, the generation and destruction of FSD was evaluated by examining the individual terms in the FSD transport equation. It was found that the creation of FSD occurs primarily in the separated shear layer region and stretched regions of the flame close to the bluff-body flameholder. The destruction of the FSD however occurs mainly at the subgrid scales, concentrating in regions where flame rollup and flow reversal take place. These features demonstrate the importance of non-equilibrium effects between the generation and destruction of local FSD in the Volvo afterburner experiment.

8. Acknowledgements

The authors would like to acknowledge financial support from the Dorothy Hodgkin Postgraduate Award and Rolls-Royce Plc.

References

[1] H. Pitsch. Large-eddy simulation of turbulent combustion. *Annual Review of Fluid Mechanics*, 38:453–482, 2006.

[2] E. R. Hawkes and R. S. Cant. A flame surface density approach to LES of premixed turbulent combustion. *Proceedings of the Combustion Institute*, 28:51–58, 2000.

[3] E. R. Hawkes and R. S. Cant. Implications of a flame surface density approach to large eddy simulation of premixed turbulent combustion. *Combustion and Flame*, 126:1617–1629, 2001.

[4] F. Charlette, A. Trouvé, M. Boger, and D. Veynante. A power-law flame wrinkling model for LES of premixed turbulent combustion Part I : Non-dynamic formulation and initial tests. *Combustion and Flame*, 131:159–180, 2002.

[5] H. G. Weller, G. Tabor, A.D. Gosman, and C. Fureby. Application of a flame-wrinkling LES combustion model to a turbulent mixing layer. *Symposium (International) on Combustion*, 27:899–907, 1998.

[6] W-W Kim and S. Menon. Numerical modeling of turbulent premixed flames in the thin-reaction-zones regime. *Combustion Science and Technology*, 160:119–150, 2000.

[7] H. Pitsch and L. Duchamp de Lageneste. Large-eddy simulation of premixed turbulent combustion using a level-set approach. *Proceedings of the Combustion Institute*, 29:2001–2008, 2002.

[8] P. Domingo, L. Vervisch, S. Payet, and R. Hauguel. DNS of a premixed turbulent V flame and LES of a ducted flame using a FSD-PDF subgrid scale closure with FPI-tabulated chemistry. *Combustion and Flame*, 143:566–586, 2005.

[9] O. Colin, F. Ducros, D. Veynante, and T. J. Poinsot. A thickened flame model for large eddy simulations of turbulent premixed combustion. *Physics of Fluids*, 12:1843–1863, 2000.

[10] M. Boger, D. Veynante, H. Boughanem, and A Trouvé. Direct numerical simulation analysis of flame surface density concept for large eddy simulation of turbulent premixed combustion. *Symposium (International) on Combustion*, 27:917–925, 1998.

[11] S. S. Ibrahim, S. R. Gubba, A. R. Masri, and W. Malalasekera. Calculations of explosion deflagrating flames using a dynamic flame surface density model. *Journal of Loss Prevention in the Process Industries*, 22(3):258–264, 2009.

[12] G. Wang, M. Boileau, and D. Veynante. Implementation of a dynamic thickened flame model for large eddy simulations of turbulent premixed combustion. *Combustion and Flame*, 158(11):2199–2213, 2011.

[13] T. Schmitt, A. Sadiki, B. Fiorina, and D. Veynante. Impact of dynamic wrinkling model on the prediction accuracy using the F-TACLES combustion model in swirling premixed turbulent flames. *Proceedings of the Combustion Institute*, 34(1):1261–1268, 2013.

[14] A. Hosseinzadeh, A. Sadiki, and J. Janicka. Assessment of the Dynamic SGS Wrinkling Combustion Modeling Using the Thickened Flame Approach Coupled with FGM Tabulated Detailed Chemistry. *Flow, Turbulence and Combustion*, (96):939–964, 2016.

[15] S. B. Pope. The evolution of surfaces in turbulence. *International Journal of Engineering Science*, 26:445–469, 1988.

[16] S. M. Candel and T. J. Poinsot. Flame stretch and the balance equation for the flame area. *Combustion Science and Technology*, 70:1–15, 1990.

[17] N. Chakraborty and R. S. Cant. Direct numerical simulation analysis of the flame surface density transport equation in the context of large eddy simulation. *Proceedings of the Combustion Institute*, 32:1445–1453, 2009.

[18] N. Chakraborty and R. S. Cant. Influence of Lewis number on strain rate effects in turbulent premixed flame propagation. *International Journal of Heat and Mass Transfer*, 49:2158–2172, 2006.

[19] N. Chakraborty, M. Klein, and R. S. Cant. Effects of turbulent reynolds number on the displacement speed statistics in the thin reaction zones regime of turbulent premixed combustion. *Journal of Combustion*, 2011:1–19, 2011.

[20] N. Chakraborty and R. S. Cant. A priori analysis of the curvature and propagation terms of the flame surface density transport equation for large eddy simulation. *Physics of Fluids*, 19:1–22, 2007.

[21] N. Shahbazian, C. P. T. Groth, and Ö L. Gülder. Comparative study of algebraic and transported FSD models for LES of premixed flames in flamelet and thin reaction zones regimes. *51st AIAA Aerospace Sciences Meeting, Grapevine, Texas, January, AIAA 2013–1138*, pages 1–13, 2013.

[22] C. Fureby. A computational study of combustion instabilities due to vortex shedding. *Proceedings of the Combustion Institute*, 28:783–791, 2000.

[23] G. Lecocq, S. Richard, O. Colin, and L. Vervisch. Gradient and counter-gradient modeling in premixed flames: theoretical study and application to the LES of a lean premixed turbulent swirl-burner. *Combustion Science and Technology*, 182:465–479, 2010.

[24] T. Ma, O. T. Stein, N. Chakraborty, and A. M. Kempf. A posteriori testing of the flame surface density transport equation for LES. *Combustion Theory and Modelling*, 18:32–64, 2014.

[25] F. E. Hernández-Pérez, F. T C Yuen, C. P T Groth, and Ö L. Gülder. LES of a laboratory-scale turbulent premixed Bunsen flame using FSD, PCM-FPI and thickened flame models. *Proceedings of the Combustion Institute*, 33:1365–1371, 2011.

[26] S. Richard, O. Colin, O. Vermorel, a. Benkenida, C. Angelberger, and D. Veynante. Towards large eddy simulation of combustion in spark ignition engines. *Proceedings of the Combustion Institute*, 31:3059–3066, 2007.

[27] A. Sjunnesson, S. Olovsson, and S. Sjöblom. Validation rig - A tool for flame studies. *In ISABE Conference, Nottingham, UK*, 1991.

[28] A. Sjunnesson, A. Olovsson, and E. Max. Measurements of velocities and turbulence in a bluff body stabilized flame. *In Fourth International Conference on Laser Anemometry - Advances and Application, ASME Cleveland, US*, 1991.

[29] A. Sjunnesson, P. Henrikson, and C. Lofstrom. CARS measurement and visualization of reacting flow in a bluff body stabilized flame. *AIAA/SAE/ASME/ASEE 28th Joint Propulsion Conference and Exhibit, July 6-8, Nashville, TN*, 1992.

[30] S. J. Shanbhogue, S. Husain, and T. Lieuwen. Lean blowoff of bluff body stabilized flames: Scaling and dynamics. *Progress in Energy and Combustion Science*, 35:98–120, 2009.

[31] R. R. Erickson and M. C. Soteriou. The influence of reactant temperature on the dynamics of bluff body stabilized premixed flames. *Combustion and Flame*, 158:2441–2457, (2011).

[32] C.Y. Lee, L. K. B. Li, M. P. Juniper, and R. S. Cant. Nonlinear hydrodynamic and thermoacoustic oscillations of a bluff-body stabilised turbulent premixed flame. *Combustion Theory and Modelling*, 20:1–23, 2016.

[33] P. Nilsson and X.S. Bai. Effects of flame stretch and wrinkling on co formation in turbulent premixed combustion. *Proceedings of the Combustion Institute*, 29:1873–1879, 2002.

[34] E. Giacomazzi, V. Battaglia, and C. Bruno. The coupling of turbulence and chemistry in a premixed bluff-body flame as studied by LES. *Combustion and Flame*, 138:320–335, 2004.

[35] I. Porumbel and S. Menon. Large eddy simulation of bluff body stabilized premixed flame. *44th AIAA Aerospace Sciences Meeting and Exhibit 9-12 January 2006, Reno, Nevada*, (January), 2006.

[36] B. Manickam, J. Franke, S. P. R. Muppala, and F. Dinkelacker. Large-eddy simulation of triangular-stabilized lean premixed turbulent flames: quality and error assessment. *Flow, Turbulence and Combustion*, 88:563–596, 2012.

[37] W. P. Jones, A. J. Marquis, and F. Wang. Large eddy simulation of a premixed propane turbulent bluff body flame using the Eulerian stochastic field method. *Fuel*, 140:514–525, 2015.

[38] P. A. T. Cocks, M. C. Soteriou, and V. Sankaran. Impact of numerics on the predictive

capabilities of reacting flow LES. *Combustion and Flame*, 162:3394–3411, 2015.

[39] A. M Briones, B. Sekar, and H. Thornburg. *Proceedings of ASME Turbo Expo, Vancouver, Canada, GT2011-45089*.

[40] C. Fureby. Large eddy simulation of combustion instabilities in a jet engine afterburner model. *Combustion Science and Technology*, 161:213–243, 2000.

[41] A. Ghani, T. Poinsot, L. Gicquel, and G. Staffelbach. LES of longitudinal and transverse self-excited combustion instabilities in a bluff-body stabilized turbulent premixed flame. *Combustion and Flame*, 162:4075–4083, 2015.

[42] H-G. Li, P. Khare, H-G. Sung, and V. Yang. A LES study of combustion dynamics of bluff-body stabilized flames. *Combustion Science and Technology*, 2202, 2016.

[43] R. D. Smagorinsky. General circulation experiment with the primitive equations. *Monthly Weather Review*, 91:99–164, 1963.

[44] B. J. Daly and H. H. Francis. Transport equations in turbulence. *Physics of Fluids*, 13:2634–2649, 1970.

[45] E. R. Hawkes and R. S. Cant. Physical and numerical realizability requirements for flame surface density approaches. *Proceedings of the Combustion Institute*, 5:699–720, 2001.

[46] J. Duclos, D. P. Veynante, and T. J. Poinsot. A comparison of flamelet models for premixed turbulent combustion. *Combustion and Flame*, 95:101–117, 1993.

[47] C. Meneveau and T. J. Poinsot. Stretching and quenching of flamelets in premixed turbulent combustion. *Combustion and Flame*, 86:311–332, 1991.

[48] C. Angelberger, D. Veynante, F. Egolfopoulos, and T. J. Poinsot. Large eddy simulations of combustion instabilities in premixed flames. *Research Proceedings of the Summer Program. CTR, Stanford*, 1998.

[49] H. G. Weller, G. R. Tabor, H. Jasak, and C. Fureby. A tensorial approach to computational continuum mechanics using object-oriented techniques. *Comput. Phys.*, 12:620–631, 1998.

[50] C. M. Rhie and W. L. Chow. Numerical study of the turbulent flow past an airfoil with trailing edge separation. *AIAA Journal*, 21:1525–1532, 1983.

[51] R. I. Issa. Solution of the implicitly discretised fluid flow equations by operator-splitting. *Journal of Computational Physics*, 62:40–65, 1985.

[52] N. Kornev and E. Hassel. Method of random spots for generation of synthetic inhomogeneous turbulent fields with prescribed autocorrelation functions. *Communication in Numerical Methods in Engineering*, 23:35–43, 2007.

[53] T. J. Poinsot and S. K. Lele. Boundary conditions for direct simulations of compressible viscous flows. *J. Comp. Phys.*, 101:104–129, 1992.

[54] T Poinsot and D. Veynante. *Theoretical and Numerical Combustion*. Edwards, Reston, VA, USA, 2005.

[55] J. C. R. Hunt, A. A. Wray, and P. Moin. Eddies, streams, and convergence zones in turbulent flows. *Center for Turbulence Research Proceedings of the Summer Programme*, 1988.

[56] R. W. Metcalfe, S. A. Orszag, M. E. Brachet, S. Menon, and J. J. Riley. Secondary instability of a temporally growing mixing layer. *Journal of Fluid Mechanics*, 184:207–243, 2006.

[57] I. B. Celik, Z. N. Cehreli, and I. Yavuz. Index of resolution quality for large eddy simulations. *Journal of Fluids Engineering*, 127:949–958, 2005.

[58] S. B. Pope. Ten questions concerning the large-eddy simulation of turbulent flows. *New journal of Physics*, 6:35, 2004.

[59] S. Shanbhogue, D-H Shin, S. Hemchandra, D. Plaks, and T. Lieuwen. Flame sheet dynamics of bluff-body stabilized flames during longitudinal acoustic forcing. *Proceedings of the Combustion Institute*, 32:1787–1794, 2009.

[60] D-H Shin and T. Lieuwen. Flame wrinkle destruction processes in harmonically forced, turbulent premixed flames. *Journal of Fluid Mechanics*, 721:484–513, 2013.